http://dx.doi.org/10.1016/j.spmi.2019.05.004

Simulation study for the current matching optimization in $In_{0.48}Ga_{0.52}N/In_{0.74}Ga_{0.26}N$ dual junction solar cells

Y. Marouf [1], L. Dehimi [1,2], and F. Pezzimenti[3,*]

[1]*Laboratory of Metallic and Semiconductor Materials, University of Biskra, Algeria.*
[2]*Faculty of Science, University of Batna, Algeria.*
[3]*DIIES – Mediterranea University of Reggio Calabria, Italy.*
[*]*Corresponding author: F. Pezzimenti, fortunato.pezzimenti@unirc.*

Abstract

In this paper indium gallium nitride (InGaN) is used to design and optimize a dual junction (DJ) solar cell, which is series-connected via a tunnel diode, with a careful analysis of the current matching between the top and the bottom sub-cells. In particular, a bandgap combination of 1.76eV/1.13eV for an $In_{0.48}Ga_{0.52}N/In_{0.74}Ga_{0.26}N$ structure is adopted and several numerical simulation results are presented. The doping concentration and the base thickness of each sub-cell are considered as fitting parameters in order to determine an accurate current matching condition. The $In_{0.48}Ga_{0.52}N$-based n^{++}/p^{++} tunnel junction behavior is also taken into account. A maximum short circuit current density of 19.543 mA/cm^2 is obtained for a 1μm-thick base in both the sub-cells, and a p/n doping ratio of 5×10^{18} cm^{-3}/5×10^{15} cm^{-3} and 1.9×10^{19} cm^{-3}/1.9×10^{16} cm^{-3} for the top and the bottom cell, respectively. The optimized DJ solar cell exhibits an open circuit voltage of 1.713 V, a fill factor of 82.49%, and a conversion efficiency of 28.78%. The external quantum efficiency and the current (power) density-voltage characteristics of different devices are investigated in detail.

Keywords: InGaN, dual cell, tunnel junction, current matching, numerical simulation.

1. Introduction

The primary limitation in the design of high conversion efficiency solar cells, which are able to utilize the whole solar spectrum, is due to the fact that single p/n junctions can convert to electricity only the sunlight absorbed at a specific and limited range of photon energies lying close to the semiconductor bandgap. To exploit the solar spectrum very profitably and reach high efficiency results, single p/n junctions are integrated in multi-junction solar cells (MJSCs) based on mechanically stacked structures [1,2] or monolithic tandem systems [3,4] where the bandgap of each sub-cell is tailored to a different range of photon energies. Hence, MJSCs are useful to capture photons efficiently over a much wider spectral range.

The main technological issues in the MJSC design are the current and lattice mismatches between the sub-cells that reduce the conversion efficiency significantly. These issues are addressed in the monolithic approach by introducing a tunnel junction (TJ) which connects the n-terminal of one sub-cell to the p-terminal of the adjacent sub-cell. On the other hand, the mechanically stacked structures circumvent the design challenges introduced above but they present some important drawbacks due to the complexity of a low-cost integration of the single sub-cells with minimal optical losses [5].

At this time, MJSCs are based on two or three junctions of different materials connected in series [6]. Practically, there are only few semiconductors that can be employed to realize these cells, namely ternary, quaternary, and pentanary alloys showing similar physical properties such as the thermal coefficient, electron affinity, and lattice matching [7-10]. For example, the most widely used MJSCs are III–V-based like the GaInP/GaAs/Ge triple-junction, and the GaInP/GaAs and the InGaN/Si dual-junction designs that allow remarkable conversion efficiency results. However, these tandem systems suffer for the use of expensive III–V substrates and/or unmatched Si and Ge sub-cells with an indirect bandgap energy [11-14].

Moving from the considerations introduced above, in this paper we study the opportunity of designing DJ structures entirely based on indium gallium nitride (InGaN) which in fact, thanks to its attractive properties for photovoltaics (PV) and its tunable bandgap energy, allows the realization of high-performance single junction (SJ) solar cells well suited, in principle, for tandem systems [15-18]. More in detail, we design and optimize an $In_{0.48}Ga_{0.52}N/In_{0.74}Ga_{0.26}N$ dual solar cell with an accurate modeling of the current matching between the top and the bottom sub-cells that are series-connected via a n^{++}/p^{++} $In_{0.48}Ga_{0.52}N$-based TJ. A bandgap combination of 1.76eV/1.13eV for the $In_{0.48}Ga_{0.52}N/In_{0.74}Ga_{0.26}N$ structure is assumed and by using the Silvaco-Atlas physical simulator [19] the doping concentration and the base thickness of each sub-cell are considered as adjustable parameters. Recent manuscript of ours, which are addressed to the modeling of different photovoltaic devices, support the adopted simulation setup [20-28].

The external quantum efficiency and the current (power) density-voltage characteristics of different solar cells are investigated at room temperature. During the simulations, we adopted a spectral irradiance consistent with the air mass 1.5 global (AM1.5G) data that refer to the American Society for Testing and Materials (ASTM) G-173 standard. In particular, by calculating the spectral irradiance numerical integral for optical wavelengths from 200 nm to 1800 nm, the assumed incident power density was 960 W/m^2. With respecting the current matching condition, the optimized dual cell design exhibits a short circuit current density (J_{sc}) of 19.543 mA/cm^2, an open circuit voltage (V_{oc}) of 1.713 V, a fill factor (FF) of 82.49%, and a conversion efficiency (η) of 28.78%. These results are compared with literature data focused on the theoretical performance of InGaN-based tandem systems.

2. Modeling and simulation

2.1 Photocurrent expression

The effective photocurrent density in a DJ solar cell is the lower value between the two photocurrent components generated in the single cells, namely J_T for the top cell and J_B for the bottom cell, given by [2,17]:

$$J_T = q\int_0^{\lambda_T} I(\lambda)\{1-exp[-\alpha_T(\lambda)t_T]\}\,d\lambda \tag{1}$$

$$J_B = q\int_0^{\lambda_T} I(\lambda)\,exp[-\alpha_T(\lambda)t_T]\,\{1-exp[-\alpha_B(\lambda)t_B]\}d\lambda + q\int_{\lambda_B}^{\lambda_T} I(\lambda)\{1-exp[-\alpha_B(\lambda)t_B]\}\,d\lambda\,. \tag{2}$$

Here, $I(\lambda)$ is the photon flux density as a function of the wavelength λ, and α_T, α_B, t_T, and t_B are the top and bottom sub-cell absorption coefficients and thicknesses, respectively. The parameter $\lambda_{T,B}$ is in the form of $\lambda_{T,B} = hc/E_{gT,B}$ where h is Planck's constant, c is the velocity of light, and E_g is the bandgap of each cell.

The device open circuit voltage V_{oc} is the sum of the single contributions:

$$V_{oc} = V_{oc,T} + V_{oc,B} = \frac{k_B T}{q}\left[ln\left(\frac{J_{sc,T}}{J_{0,T}}+1\right) + ln\left(\frac{J_{sc,B}}{J_{0,B}}+1\right)\right] \tag{3}$$

where $J_{sc,T,B}$ is the short circuit current density of the top and bottom sub-cell, q is the electron charge, k_B is Boltzmann's constant, T is the temperature, and J_0 is the reverse saturation current density given by [17,29]

$$J_0 = qn_i^2\left[\frac{D_n}{N_A L_n}\left(\frac{\frac{S_n L_n}{D_n}cosh\left(\frac{x_p}{L_n}\right)+sinh\left(\frac{x_p}{L_n}\right)}{\frac{S_n L_n}{D_n}sinh\left(\frac{x_p}{L_n}\right)+cosh\left(\frac{x_p}{L_n}\right)}\right) + \frac{D_p}{N_D L_p}\left(\frac{\frac{S_p L_p}{D_p}cosh\left(\frac{x_n}{L_p}\right)+sinh\left(\frac{x_n}{L_p}\right)}{\frac{S_p L_p}{D_p}sinh\left(\frac{x_n}{L_p}\right)+cosh\left(\frac{x_n}{L_p}\right)}\right)\right] \tag{4}$$

where x_n and x_p are the thicknesses of the n- and p-type layers, $S_{n,p}$ is the surface recombination velocity in these regions, $D_{n,p}$ and $L_{n,p}$ are the diffusion coefficient and diffusion length for electrons and holes, and

N_A and N_D are the acceptor and donor concentrations, respectively. Finally, the intrinsic carrier concentration n_i is calculated by means of the density of states for electrons (N_c) and holes (N_v) as follows:

$$n_i^2 = N_c N_v exp\left(-\frac{E_g}{k_B T}\right). \tag{5}$$

2.2 Mobility model

The following expression based on the work of Caughey and Thomas was used to model the doping and temperature-dependent carrier mobility [30]:

$$\mu_{n,p} = \mu_{1n,p}\left(\frac{T}{300}\right)^{\alpha_{n,p}} + \frac{\mu_{2n,p}\left(\frac{T}{300}\right)^{\beta_{n,p}} - \mu_{1n,p}\left(\frac{T}{300}\right)^{\alpha_{n,p}}}{1+\left(\frac{N}{N_{n,p}^{crit}\left(\frac{T}{300}\right)^{\gamma_{n,p}}}\right)^{\delta_{n,p}}} \tag{6}$$

where N is the total (local) doping concentration and $N_{n,p}^{crit}$ is the value at which the mobility is halfway between its minimum (μ_1) and maximum (μ_2) assumed at room temperature. The reference parameters for GaN and InN regions are summarized in Table 1 [31,32]. The fitting coefficients α, β, and γ are equal to 1 [32,33].

Table 1. Carrier mobility parameters.

	GaN	**InN**
μ_{1n} ($cm^2\ V^{-1}\ s^{-1}$)	295	1982.9
μ_{2n} ($cm^2\ V^{-1}\ s^{-1}$)	1460	10885
δ_n	0.71	0.7439
N_n^{crit} (10^{16} cm^{-3})	7.7	10
μ_{1p} ($cm^2\ V^{-1}\ s^{-1}$)	3.0	3.0
μ_{2p} ($cm^2\ V^{-1}\ s^{-1}$)	170	340
δ_p	2.0	2.0
N_p^{crit} (10^{17} cm^{-3})	10	8.0

2.3 Recombination models

The indirect recombination of charge carriers that occurs in presence of traps (or defects) within the semiconductors bandgap was modelled by the Shockley-Read-Hall (SRH) standard expression [34-36]:

$$R_{SRH} = \frac{np - n_i^2}{\tau_p\left(n + n_i e^{(Etrap/kT)}\right) + \tau_n\left(p + n_i e^{(-Etrap/kT)}\right)} \tag{7}$$

Where *Etrap* is the difference between the trap energy level and the intrinsic Fermi level (i.e., $Etrap = E_t - E_i$), and τ_n and τ_p are the minority carrier lifetimes. The model assumes $\tau_{n,p}$ = 6.5 ns [32], and *Etrap* = 0, namely only one trap level corresponding to the most efficient recombination center [37].

During the simulations, the Auger and the radiative (optical) recombination models were also taken into account. In particular, the first occurs when a mobile carrier is either emitted or captured through a three-particle transition in the form of [38,39]

$$R_{Auger} = C_{Augn}\left(pn^2 - nn_i^2\right) + C_{Augp}\left(np^2 - pn_i^2\right) \tag{8}$$

whereas the latter is due to the direct bandgap transition [30]:

$$R_{rad} = C_{opt}\left(np - n_i^2\right). \tag{9}$$

The Auger and radiative coefficients are $C_{Augn,p}$ = 1.4×10^{-30} cm^6/s [29] and C_{opt} = 2.4×10^{-11} cm^3/s [40], respectively.

2.4 Optical model

The complex index of refraction with its real (refractive index, n) and imaginary (extinction coefficient, k) part for the different regions in the device structure need to be specified for simulations. Unfortunately, the built-in tables of index versus wavelength for conventional semiconductors do not include the $In_xGa_{1-x}N$ ternary alloys. To overcome this problem we used the absorption coefficient model proposed in [32], i.e.

$$\alpha\ (cm^{-1}) = 10^5 \times \sqrt{C\left(E_{ph} - E_g\right) + D\left(E_{ph} - E_g\right)^2} \tag{10}$$

which links the extinction coefficient as follows:

$$k = \frac{\lambda}{4\pi}\,\alpha\,. \tag{11}$$

At the same time, in order to express the refractive index we used Adachi's model given by [17]

$$n\left(E_{ph}\right) = \sqrt{\frac{A}{\left(\frac{E_{ph}}{E_g}\right)^2}\left[2 - \sqrt{1 + \frac{E_{ph}}{E_g}} - \sqrt{1 - \frac{E_{ph}}{E_g}}\right] + B}\ . \tag{12}$$

In (10) and (12), E_{ph} is the incoming photon energy and E_g is the material bandgap dependent on the indium composition x. The x-dependence of the parameters A, B, C, and D is in the form of

$$A = 13.55x + 9.31(1 - x) \tag{13}$$

$$B = 2.05x + 3.03(1 - x) \tag{14}$$

$$C = 3.525 - 18.29x + 40.22x^2 - 37.52x^3 + 12.77x^4 \tag{15}$$

$$D = -0.6651 + 3.616x - 2.460x^2. \tag{16}$$

In particular, A and B are linearly interpolated starting from the parameters of the binary material, namely $A = 13.55$ and $B = 2.05$ for InN, and $A = 9.31$ and $B = 3.03$ for GaN, which were experimentally measured in [31,41]. Whereas, C and D are calculated from two empirical expressions [42,43] as summarized in Table 2.

Finally, we implemented a Matlab-code that calculates the refractive index and converts the absorption coefficient into the extinction coefficient generating an input text file for the Silvaco-Atlas simulator.

Table 2. Parameters used to calculate the $In_xGa_{1-x}N$ absorption coefficient.

Indium composition	C (eV^{-1})	D (eV^{-2})

1	0.69642	0.46055
0.83	0.66796	0.68886
0.69	0.58108	0.66902
0.57	0.60946	0.62182
0.5	0.51672	0.46836
0	3.52517	-0.65710

2.5. Tunnel model

In monolithically grown MJSCs, the individual sub-cells are interconnected via a tunnel diode (Esaki diode) which aids to counter the parasitic field that is formed if an n/p cell is directly grown on the surface of another n/p cell. This diode must be transparent to the wavelengths absorbed in the series-connected sub-cells to minimize the current losses resulting from light absorption. Also, it must form a low-resistance interface to ensure minimal voltage drops.

Tunneling phenomena can occur when a sufficiently high electric field originates within a p-n junction. The band energy levels may bend sufficiently to allow electrons to tunnel by internal field emission from the valence band into the conduction band, while the symmetric behavior occurs for holes. Additional carriers, therefore, transfer to the conduction and valence band.

During the simulations, 1-D tunneling was assumed and the electric field was calculated at each node of a nanometer-sized rectangular mesh that was superimposed over the device regular mesh to give the carrier recombination-generation rate along the junction. By considering each energy level (E) in the energy range determined by the semiconductor band profiles, the net tunneling current per unit area is the form of [19]

$$J(E) = \frac{qkT}{2\pi^2 h^3} T(E) \left(m_e^* \ln \left\{ \frac{1+exp\left[\left(E-E_{fl}^{e}\right)/kT\right]}{1+exp\left[\left(E-E_{fr}^{e}\right)/kT\right]} \right\} \right) \Delta E - \frac{qkT}{2\pi^2 h^3} T(E) \left(m_h^* \ln \left\{ \frac{1+exp\left[\left(E-E_{fl}^{h}\right)/kT\right]}{1+exp\left[\left(E-E_{fr}^{h}\right)/kT\right]} \right\} \right) \Delta E \quad (17)$$

where ΔE is a small energy increment, $T(E)$ is the tunneling probability, $E_{fl}^{e,h}$ is the quasi-Fermi level for electrons and holes, and the terms m_e^* and m_h^* are given by

$$m_e^* = m_0 \sqrt{m_e(x_{end})\, m_h\left(x_{beg}\right)} \quad (18)$$

$$m_h^* = m_0 \sqrt{m_e\left(x_{beg}\right)\, m_h\left(x_{end}\right)} \ . \quad (19)$$

Here, m_e and m_h are the electron and hole effective masses, m_0 is the carrier rest mass, and x_{beg} and x_{end} represent the beginning and the ending of the tunneling path calculated for each value of E.

3. Device structure and material parameters

A schematic cross section of the proposed dual-cell structure is shown in Fig. 1.

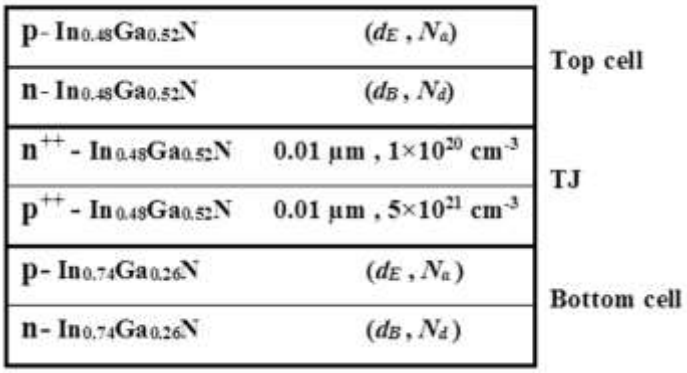

Fig. 1. $In_{0.48}Ga_{0.52}N/In_{0.74}Ga_{0.26}N$ dual cell structure.

Basically, it consists of two p-n individual sub-cells interconnected both electrically and optically via a TJ. In more detail, the tunnel diode is a highly doped $In_{0.48}Ga_{0.52}N$-based n^{++}/p^{++} junction where the n^{++} and p^{++} regions are both 10-nm-thick with a doping concentration of 1×10^{20} cm^{-3} and 5×10^{21} cm^{-3}, respectively. The top cell is also designed in $In_{0.48}Ga_{0.52}N$ whereas the bottom cell is in $In_{0.74}Ga_{0.26}N$. The doping concentrations and base thicknesses (d_B) of the top and the bottom sub-cells were considered as fitting parameters to determine an accurate current matching condition. In addition, it is important to note that all the $In_xGa_{1-x}N$ regions are arranged from bottom to top with lower to higher bandgap energies as reported in Table 3. Here, the fundamental material parameters used in the simulations for a different indium composition, such as the relative permittivity (ε), electron affinity (χ), effective density of states, and electron and hole effective masses are also listed. From Table 3, a bandgap ratio of 1.76 eV/1.13 eV is therefore calculated for the top and bottom sub-cells in Fig.1.

Table 3. InN, GaN, $In_xGa_{1-x}N$ material parameters.

	GaN	**InN**	**$In_xGa_{1-x}N$**
$E_g(eV)$ at 300 K [43]	3.42	0.77	$0.77x + 3.42(1-x) - 1.43x(1-x)$
ε [44]	8.9	15.3	$15.3x + 8.9(1-x)$
$\chi\ (eV)$ [44]	4.1	5.6	$4.1 + 0.7(3.4 - E_g)$
$N_C\ (10^{17}\mathrm{cm}^{-3})$ [44]	23	9.1	$9.1x + 23(1-x)$
$N_V\ (10^{19}\mathrm{cm}^{-3})$ [18]	4.6	5.3	$5.3x + 4.6(1-x)$
m_e [41]	0.2	0.12	$0.12x + 0.2(1-x)$
m_h [41]	1.0	0.17	$0.17x + 1.0(1-x)$

4. Results and discussion

In order to design a high efficiency DJ solar cell with a clear understanding of the different device parameters, it is necessary to optimize the performance of the single junction (SJ) sub-cells used for cascading. Hence, the top and the bottom cell considered in this work were firstly investigated separately. The calculated short circuit current density (J_{sc}), open circuit voltage (V_{oc}), and power conversion efficiency (η) of the two single cells as a function of both the emitter thickness and the acceptor concentration are shown in Fig. 2. The simulations were performed at room temperature by assuming an incident power density of 960 W/m^2 in the 200-1800 nm wavelength range.

By fixing in the paper N_a/N_d=10^3 and also d_E = 0.01 µm, the conversion efficiency behaviors of the two SJ cells as a function of both the donor concentration and the thickness of the base region are shown in Fig. 3.

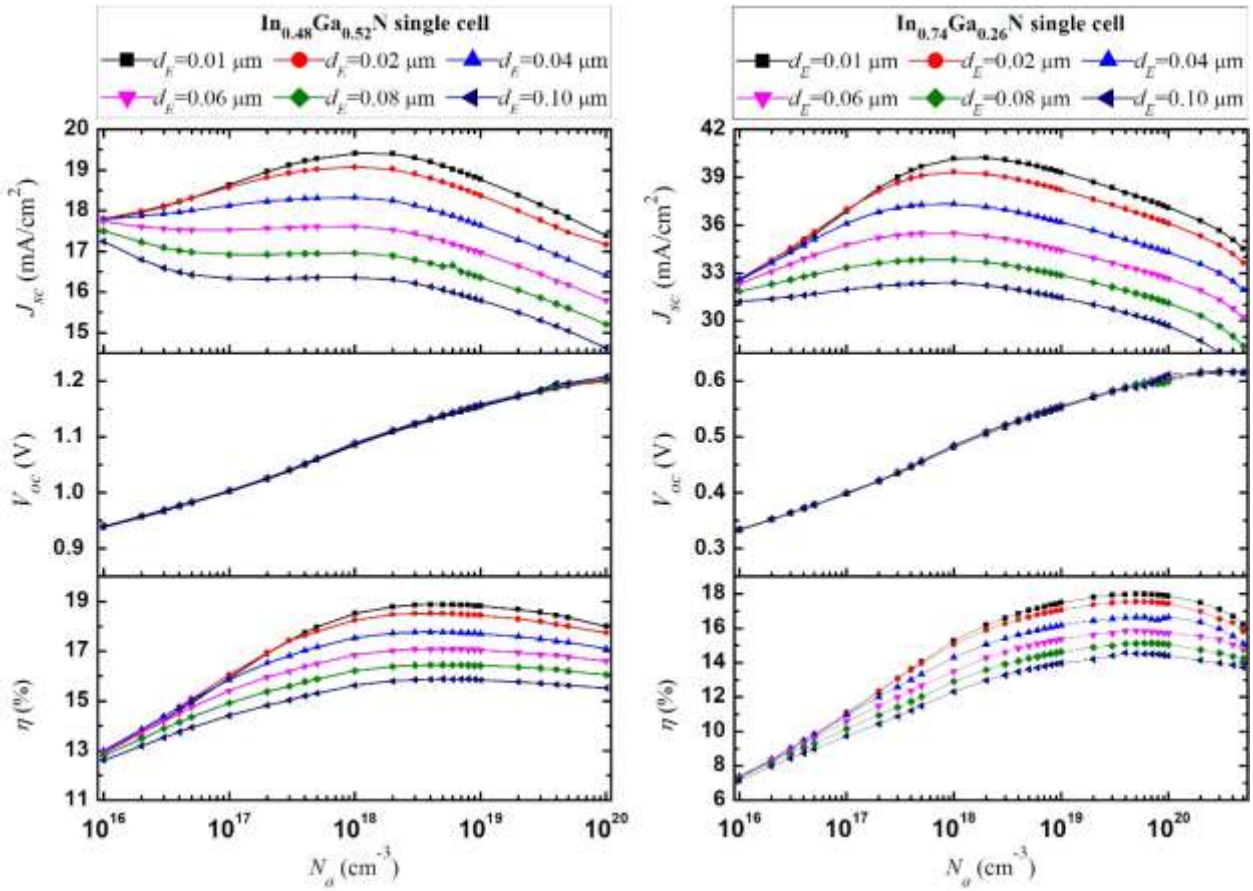

Fig. 2. Short-circuit current density J_{sc}, open-circuit voltage V_{oc}, and conversion efficiency η for the top and bottom single cell in Fig. 1. A doping concentration ratio N_a/N_d = 10^3 was imposed during the simulations and d_B = 1 µm.

From Figs. 2 and 3, the calculated photovoltaic parameters, which maximize the conversion efficiency, are summarized in Table 4.

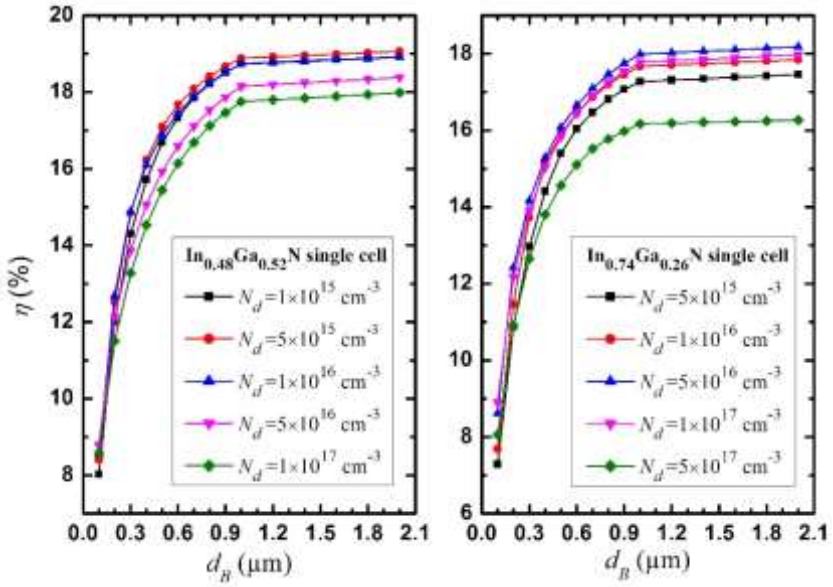

Fig. 3. Conversion efficiency as a function of the base thickness for different values of the donor doping concentration. $N_a/N_d=10^3$ and $d_E = 0.01$ μm.

Table 4. Single junction solar cell results.

SJ solar cell	J_{sc}(mA/cm^2)	V_{oc}(V)	FF(%)	η(%)	Emitter		Base	
					d_E (μm)	N_a (cm^{-3})	d_B (μm)	N_d (cm^{-3})
$In_{0.48}Ga_{0.52}N$	19.1052	1.135	83.65	18.89	0.01	5×10^{18}	1.00	5×10^{15}
$In_{0.74}Ga_{0.26}N$	37.8340	0.590	77.30	17.99	0.01	5×10^{19}	1.00	5×10^{16}

Moving from the simulation results reported above, the DJ solar cell design was optimized taking into account the current matching condition between the two sub-cells.

The energy band diagram of the DJ structure versus the distance from the top surface, namely from the $In_{0.48}Ga_{0.52}N$ wide bandgap top cell (E_g = 1.76 eV) to the narrow energy value in the $In_{0.74}Ga_{0.26}N$ bottom cell (E_g = 1.13 eV), is plotted in Fig. 4 (a).

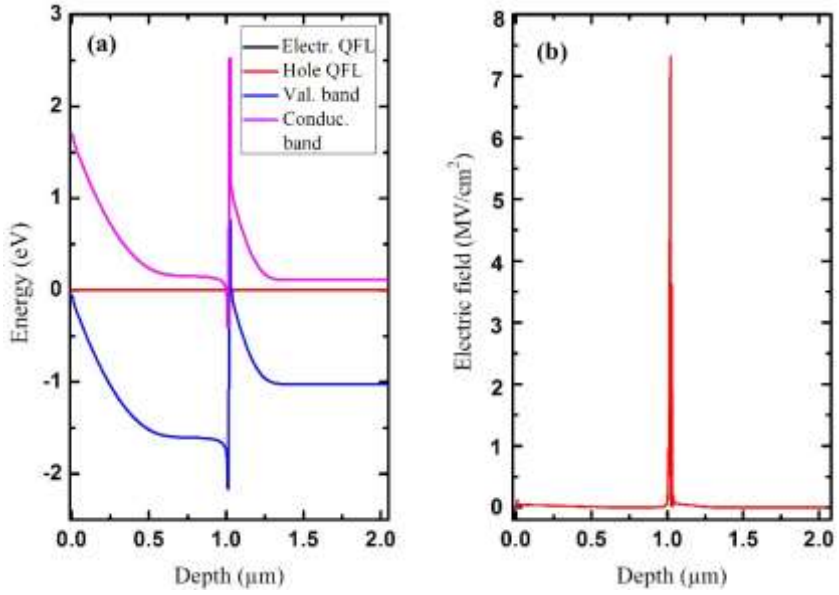

Fig. 4. (a) Energy band diagram. (b) Electric field profile.

As we can see, the tunnel junction is located at ~1.02 μm. Here, the quasi Fermi levels tend to penetrate into the conduction and the valence band determining a tunneling region that leads to the carrier recombination phenomena between the two sub-cells. This scenario is supported by the cutline view of the electric field profile along the device as shown in Fig. 4 (b) which exhibits a maximum value just across the tunnel junction.

In order to guarantee the current matching requirement, the effect of some fundamental geometrical and physical parameters was investigated in detail. In particular, the base layer thickness for both the sub-cells was assumed in the range 0.5-1.5 μm. At the same time, the acceptor doping concentration in the emitter region was ranged from 1×10^{17} cm^{-3} to 1×10^{20} cm^{-3} in the top cell and from 1×10^{18} cm^{-3} to 5×10^{19} cm^{-3} in the bottom cell. The J_{sc} behaviors of different SJ and DJ designs are shown in Figs. 5-7. From Figs. 5 and 6, we can see that the J_{sc} curves of the dual cell design are always determined by the top cell current capabilities. In particular, from Fig. 5, these curves increase with increasing the top cell acceptor concentration, reach a maximum value and then decrease for $N_{a\,(top)}$ exceeding 5×10^{18} cm^{-3} as a consequence of high-doping effects in terms of carrier mobility degradation (6). At the same time, the DJ J_{sc} behaviors are almost independent from the acceptor doping concentration in the bottom cell. By considering that the bottom cell J_{sc} decreases with increasing the $N_{a\,(bot)}$ concentration, in the DJ structure an almost perfect current matching value of 19.553 mA/cm^2 is obtained in Fig. 5 (d) for $N_{a\,(top)} = 5\times10^{18}$ cm^{-3} and $N_{a\,(bot)} = 1.9\times10^{19}$ cm^{-3}. On the other hand, from Fig. 6, the bottom cell J_{sc} increases for increasing values of the acceptor concentration, reaches a maximum of 21.2 mA/cm^2 and then decreases for $N_{a\,(bot)}$ exceeding 1×10^{18} cm^{-3}. At the same time, the DJ J_{sc} is slightly dependent on $N_{a\,(bot)}$.

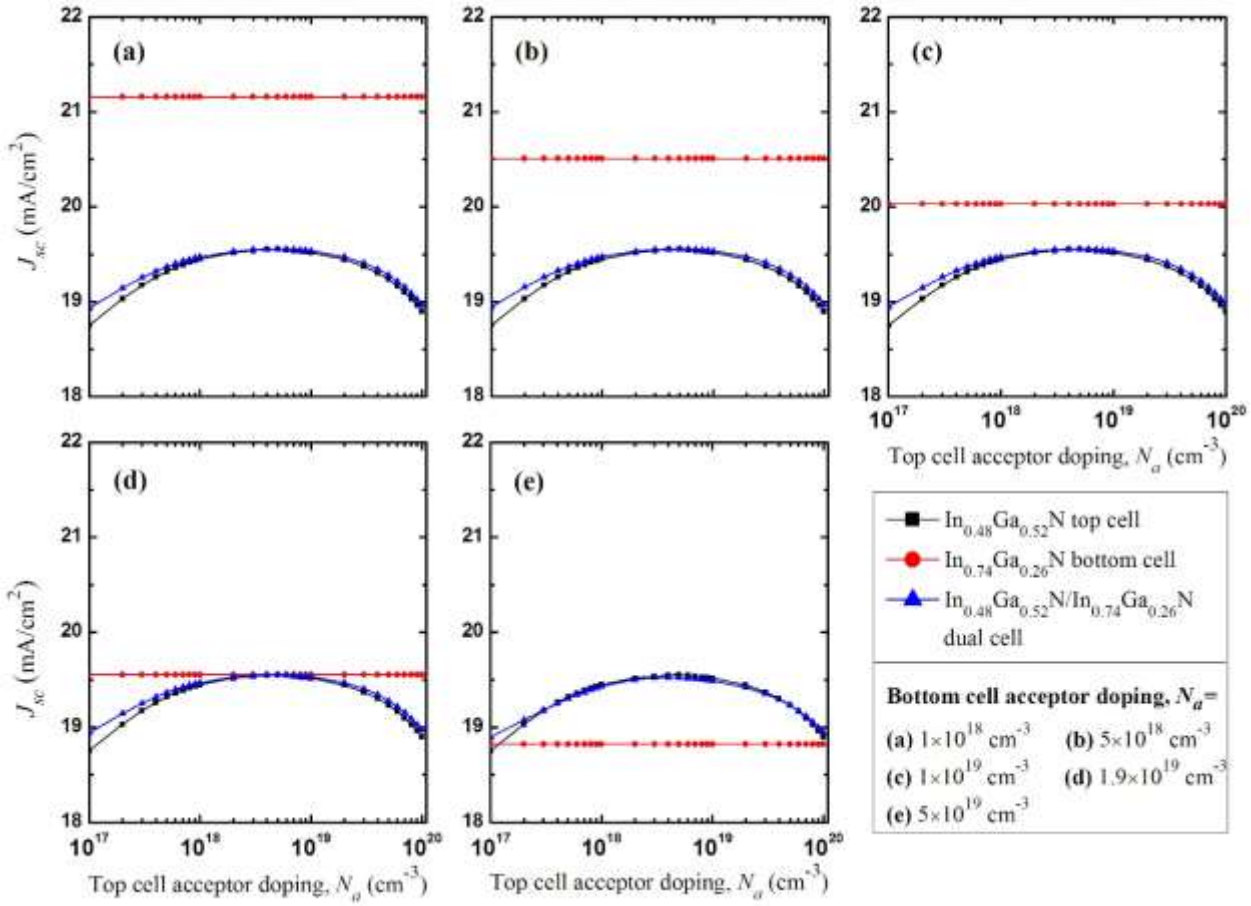

Fig. 5. J_{sc} as a function of the top cell acceptor concentration for different values of N_a in the bottom cell. In each sub-cell $N_a/N_d=10^3$, d_B = 1 μm, and d_E = 0.01 μm.

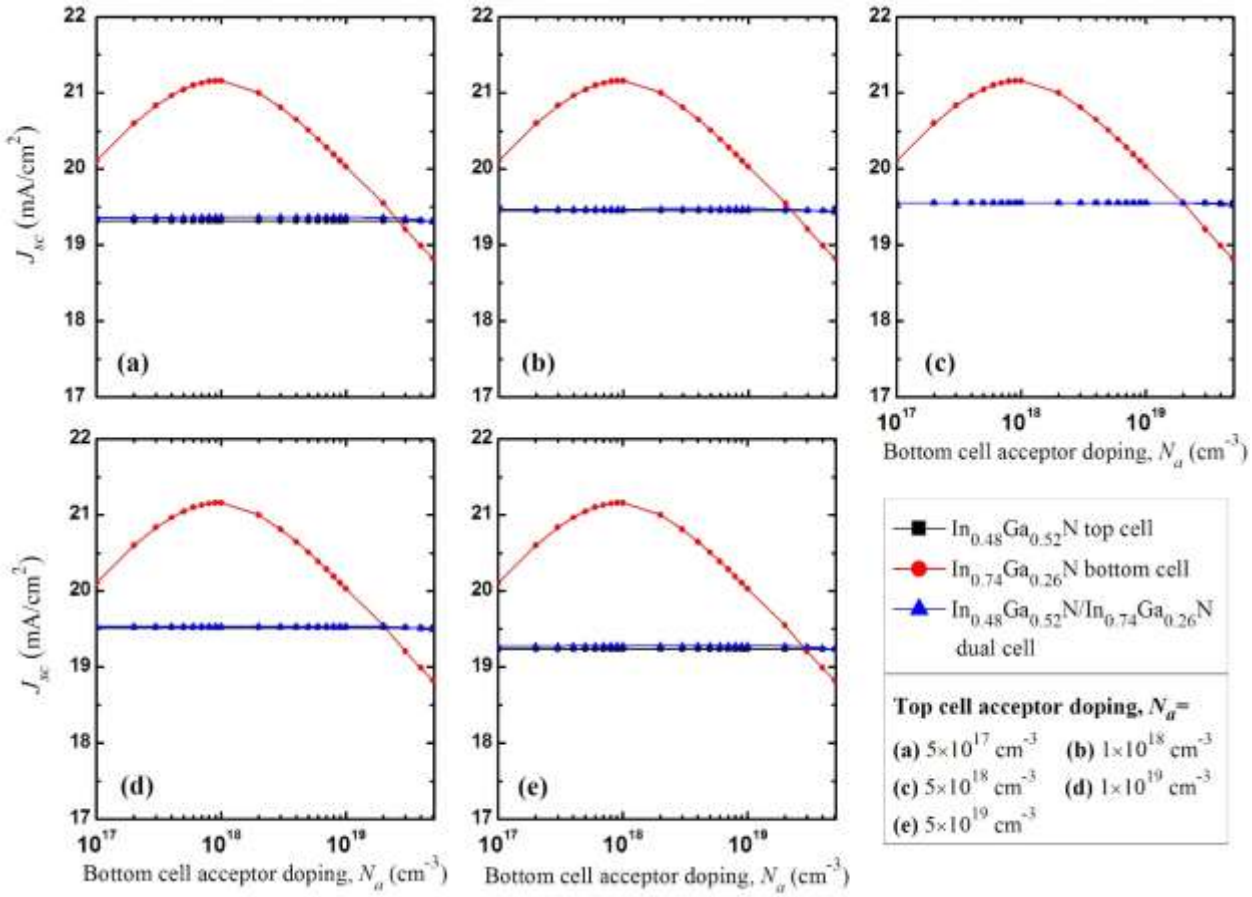

Fig. 6. J_{sc} as a function of the bottom cell acceptor concentration for different values of N_a in the top cell. In each sub-cell $N_a/N_d=10^3$, d_B = 1 μm and d_E = 0.01 μm.

Figure 7 shows the J_{sc} behaviors versus the top and bottom cell base thickness. As we can note, the top cell J_{sc} increases with increasing the top cell base thickness $d_{B\,(top)}$. Also, by increasing $d_{B\,(bot)}$, the DJ J_{sc} curve more and more tends to overlap with that of the top cell, and for $d_{B\,(bot)} \geq 0.9$ μm the two curves can be considered coincident. In addition, the bottom cell J_{sc} behavior decreases as $d_{B\,(top)}$ increases (shadowing effect) and also for a thinner $d_{B\,(bot)}$.

Summarizing the previous results, it is evident that the current matching condition in the DJ structure is achieved in correspondence of fine-tuned geometrical and physical parameters. For example, starting from the reference $In_{0.48}Ga_{0.52}N$ SJ cell in Table 4 as top cell, we can perform a DJ optimized design assuming a bottom cell with an emitter acceptor concentration of 1.9×10^{19} cm^{-3} and 1-μm-thick base region. In our calculations, this doping level corresponds to a base donor concentration of 1.9×10^{16} cm^{-3}.

The useful wavelength range of the proposed design can be determined by plotting the external quantum efficiency (EQE) behavior of the top, bottom, and dual cell as shown in Fig. 8. The $EQE(\lambda)$ was defined as the ratio of the effective photocurrent calculated through the solar cell divided by the source photocurrent imposed during the simulations. This latter is in the form of $I_{src} = q\lambda P_B W_B/hc$ where P_B is the power density of the incident beam and W_B is the beam width clipped to the device structure.

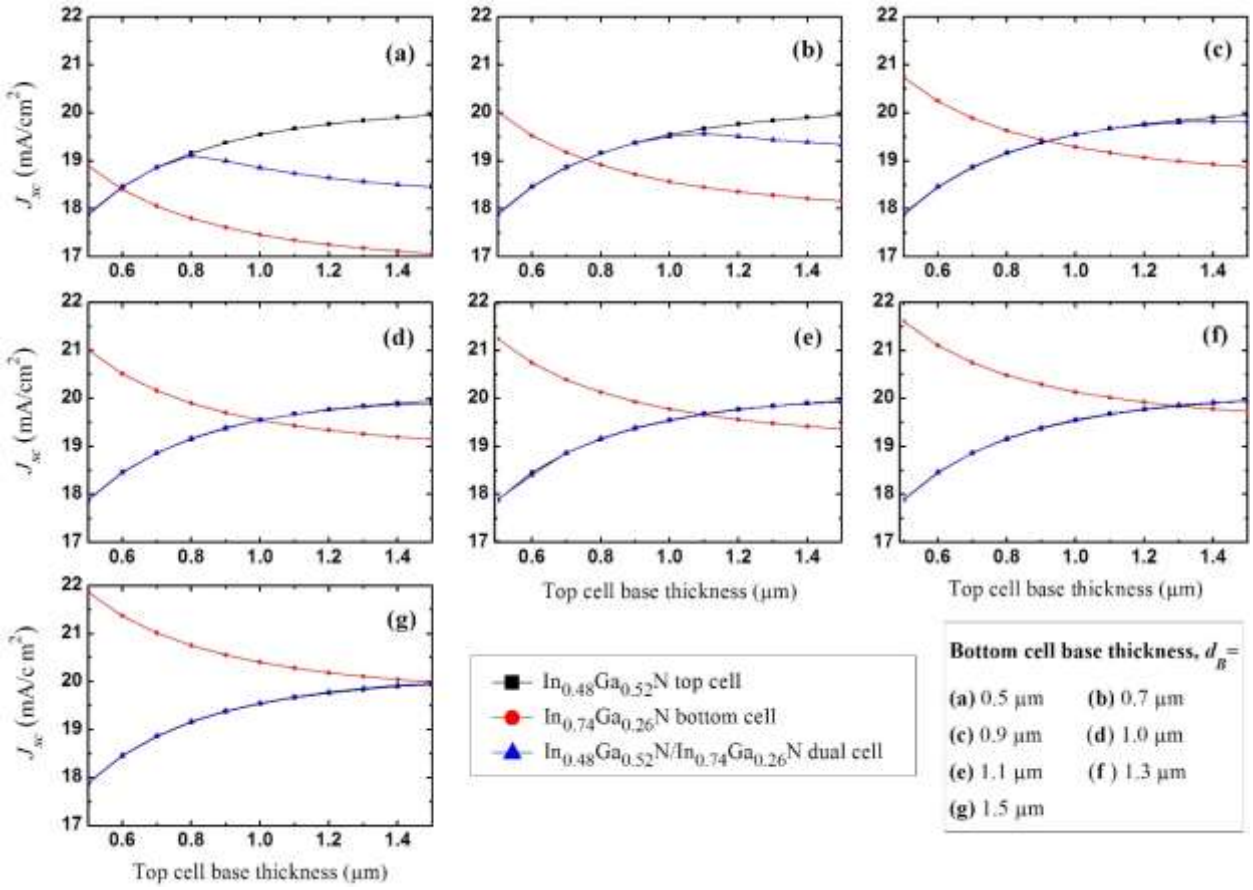

Fig. 7. J_{sc} as a function of the top cell base thickness for different values of d_B in the bottom cell. $N_{a(\text{top})} = 5\times10^{18}$ cm^{-3}, $N_{a\,(\text{bot})} = 1.9\times10^{19}$ cm^{-3}, and $d_E = 0.01$ μm in each sub-cell.

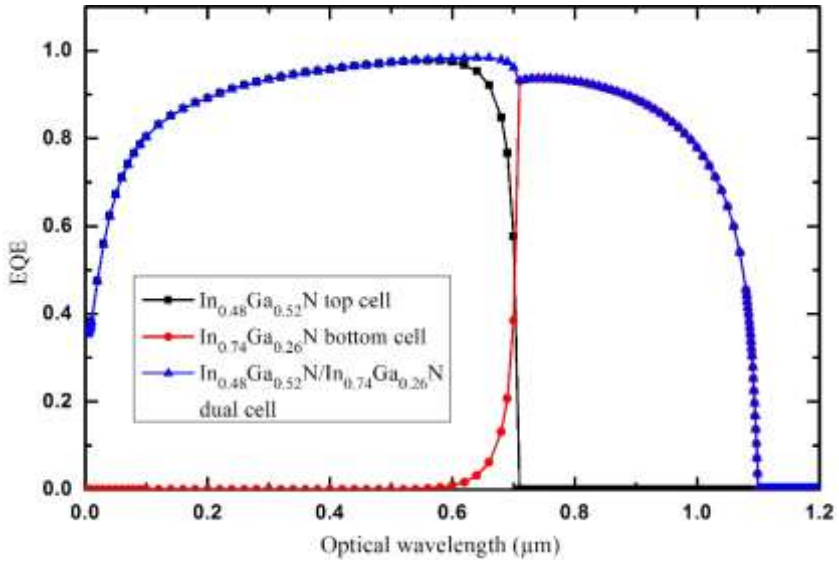

Fig. 8. External quantum efficiency of the top, bottom, and dual cell design.

The shortest wavelengths of the solar spectrum**,** which are lower than 0.69 μm, are absorbed by the $In_{0.48}Ga_{0.52}N$ top cell with the highest bandgap material while the remaining photons are transmitted to the

bottom cell. At the same time, the longest solar spectrum wavelengths in the range of 0.69-1.1 μm are absorbed by the $In_{0.74}Ga_{0.26}N$ bottom cell with the narrowest bandgap. From Fig. 8, we can see that the maximum absorption of the DJ structure occurs within the 0.1-1 μm wavelength range where the average EQE is around 79% with a maximum value close to 98% at 0.64 μm.

The current density-voltage (*J-V*) and the power density-voltage (*P-V*) characteristics of the different devices are shown in Fig. 9, and the extracted photovoltaic parameters are listed in Table 5.

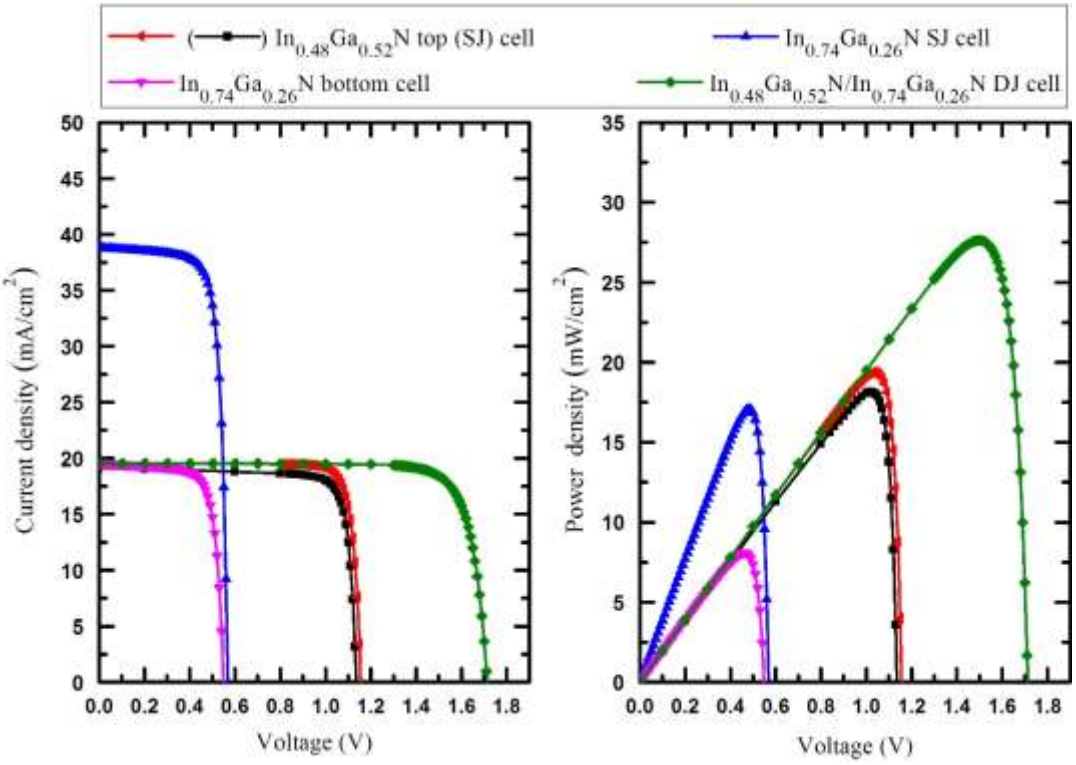

Fig. 9. (a) *J-V* and (b) *P-V* characteristics.

Table 5. Photovoltaics parameters.

Solar cells	J_{sc} (mA/cm^2)	V_{oc} (V)	FF (%)	η (%)
$In_{0.48}Ga_{0.52}N$/ $In_{0.74}Ga_{0.26}N$ DJ cell	19.5532	1.713	82.49	28.78
$In_{0.48}Ga_{0.52}N$ top cell	19.5431	1.156	85.88	20.21
$In_{0.74}Ga_{0.26}N$ bottom cell	19.5516	0.548	75.52	8.428
$In_{0.48}Ga_{0.52}N$ SJ cell	19.1052	1.135	83.65	18.89
$In_{0.74}Ga_{0.26}N$ SJ cell	38.7712	0.569	77.41	17.78

By comparing the SJ results in Table 5 with those reported in Table 4, we can note a different performance for the $In_{0.74}Ga_{0.26}N$ cell due to the different doping levels, i.e., $N_a = 1.9\times10^{19}$ cm^{-3} and $N_d = 1.9\times10^{16}$ cm^{-3}. Also, it is worthwhile noting that, although the $In_{0.48}Ga_{0.52}N$ SJ and top cell have the same geometrical and physical parameters the presence of the TJ in the DJ design determines different results. In fact, the n/n^{++} junction which originates in the top cell (see Fig. 1) acts as a back surface field interface leading to a slightly increase of the photogeneration phenomena. On the other hand, the $In_{0.74}Ga_{0.26}N$ bottom cell exhibits a sharp drop in the J_{sc} value (19.5516 mA/cm^2) if compared with the $In_{0.74}Ga_{0.26}N$ single cell result (38.7712 mA/cm^2). This is because the bottom cell absorbs only the part of spectrum transmitted by the top cell (i.e. the part of

wavelengths greater than 0.69 μm as shown in Fig. 8). At the same time, the bottom cell V_{oc} value is slightly affected by the illumination intensity and it is reduced from 0.569 V to 0.548 V.

As expected, the DJ design presents a J_{sc} value mainly limited by the current capabilities of the series-connected top cell and a V_{oc} of 1.713 V close to the sum of the V_{oc} contributions of each sub-cell since the voltage drop across the TJ is lower than 10 mV. The DJ maximum power density in Fig. 9 (b) is 27.63 mW/cm^2 at a bias voltage of 1.5 V determining a *FF* of 82.49% and a power conversion efficiency of 28.78%. This result is consistent with literature data on InGaN-based tandem solar cells and, in fact, a maximum efficiency of 27.48% was simulated for several $In_xGa_{1-x}N$ PV devices in [3]. For the sake of truth, other works reported values of η in excess of 30% [15-18]. There, however, different designs, material parameters, and physical models were used. In particular, in [15] and [16] the direct (radiative) and indirect (SRH and Auger) recombination models, which play a significant role in reducing the efficiency, were not taken into account achieving a conversion efficiency around 34%. In addition, in [17] and [18] the authors introduced additional layers in the device structure, such as antireflection coating, back surface field, and transparent conductive oxide interfaces to improve the conversion efficiency with a noticeable record in the order of 35%.

5. Conclusion

We have investigated the design of an $In_{0.48}Ga_{0.52}N/In_{0.74}Ga_{0.26}N$ DJ solar cell in the 0.2-0.8 μm wavelength range by means of a numerical simulation study. A bandgap combination of 1.76eV/1.13eV has been assumed in the device structure. The geometrical and doping parameters of the different emitter and base regions have been carefully tuned to achieve the maximum short circuit current density determining an almost perfect current matching condition. The impact of the TJ has also been evaluated.

The computed PV parameters extracted from the DJ *J-V* and *P-V* characteristics are J_{sc} = 19.553 mA/cm^2, V_{oc} = 1.713 V, *FF* = 82.49%, and η = 28.78%. The obtained results have been compared with literature data and turn useful to support the modelling efforts aimed at designing InGaN-based MJSCs by considering that the pure experimental optimization of these structures could be too expensive and time consuming.

References

[1] S. Yoshidomi, J. Furukawa, M. Hasumi, T. Sameshima, Enrgy Proced. 60, 116 (2014).

[2] Z. Li, H. Xiao, X. Wang, C. Wang, Q. Deng, L. Jing, X. Hou, Physica B 414, 110 (2013).

[3] H. Hamzaoui. A. S. Bouazzi, B. Rezig, Sol. Energ. Mat. Sol. C. 87, 595 (2005).

[4] L. Hsu, W. Walukiewicz, J. Appl. Phys. 104, 024507 (2008).

[5] S. Nacer, A. Aissat, J. Appl. Phys. A, 122, 138 (2016).

[6] M.A. Green, K. Emery, Y. Hishikawa, W. Warta, E.D. Dunlop, D.H. Levi, A. W.Y. Ho-Baillie, Prog. Photovolt: Res. Appl. 25, 3 (2017).

[7] B. Gil, Group III Nitride Semiconductor Compounds, Physics and Applications, Clarendon Press, NY, 1998.

[8] G.R. Yazdi, P.O.A Persson, D. Gogova, R. Fornari, L. Hultman, M. Syväjärvi, R. Yakimova, Nanotechnology 20, 495304 (2009).

[9] K. Chakir, C. Bilel, M.M. Habchi, A. Rebey, Superlattice. Microst. 102, 56-63 (2017).

[10] Ö. Akıncı, H.H. Gürel, H. Ünlü, Superlattice. Microst. 36, 685-692 (2004).

[11] M. Yamagushi, Sol. Energ. Mat. Sol. C. 75, 261 (2003).

[12] N. Jain, M.K. Hudait, IEEE J. Photovolt. 3, 528 (2013).

[13] H. Bencherif, L. Dehimi, F. Pezzimenti, A. Yousfi, Proc. 2018 International Conference on Applied Smart Systems, ICASS, 8651990 (2019).

[14] F. Bouzid, F. Pezzimenti, L. Dehimi, F.G. Della Corte, M. Hadjab, A. Hadj Larbi, J. Electron. Mater. 48, 14107 (2019).

[15] A. Mesrane, A. Mehrane, F. Rahmoune, A. Oulebsir, J. Electron Mater. 46, 1458 (2017).

[16] X. Shen, S. Lin, F. Li, Y. Wei, S. Zhong, H. Wan, J. Li, Proc. SPIE, 7045, 70450 (2008).

[17] X. Zhang, X. Wang, H. Xiao, C. Yang, J. Ran, C. Wang, Q. Hou, J. Li, Z. Wang, J. Phys. D: Appl. Phys. 41, 245104 (2008).

[18] N. Akter, Int. J. Res. Eng. Tech. 3, 315 (2014).

[19] Silvaco Int., Atlas User's Manual, Device Simulator Software (2013).

[20] Y. Marouf, L. Dehimi, F. Bouzid, F. Pezzimenti, F.G. Della Corte, Optik, 163, 22 (2018).

[21] F.G. Della Corte, G. De Martino, F. Pezzimenti, G. Adinolfi, G. Graditi, IEEE Trans. Electron Dev. 68, 3352 (2018).

[22] F. Bouzid, L. Dehimi, F. Pezzimenti, J. Electron Mater. 46, 6563 (2017).

[23] G. De Martino, F. Pezzimenti, F.G. Della Corte, G. Adinolfi, G. Graditi, Proc. 13th Conf. on PhD Research in Microelectronics and Electronics, PRIME, 221-224 (2017).

[24] F. Bouzid, F. Pezzimenti, L. Dehimi, M. L. Megherbi, F.G. Della Corte, Jpn. J. Appl. Phys. 56, 094301 (2017).

[25] G. De Martino, F. Pezzimenti, F. G. Della Corte, Proc. International Semiconductor Conference – CAS, 147-150 (2018).

[26] H. Bencherif, L. Dehimi, F. Pezzimenti, F. G. Della Corte, Appl. Phys. A-Mater. 125, 294 (2019).

[27] F. Bouzid, L. Dehimi, F. Pezzimenti, M. Hadjab, A.H. Larbi, Superlattice. Microst. 122, 57 (2018).

[28] H. Bencherif, L. Dehimi, F. Pezzimenti, F.G. Della Corte, Optik 182, 682 (2019)

[29] S.R. Kurtz, P. Faine, J. M. Olson, J. Appl. Phys. 68, 1890 (1990).

[30] F. Schwierz, Solid State Electron. 49, 889 (2005).

[31] Y.C. Shen, G.O. Mueller, S. Watanabe, N.F. Gardner, A. Munkholm, M.R. Krames, Appl. Phys. Lett. 91, 141101 (2007).

[32] G. Brown, J. Ager III, W.Walukiewicz, J. Wu, Sol. Energ. Mat. Sol. C. 94, 478 (2010).

[33] X. Zhang, X. Wang, H. Xiao, C. Yang, J. Ran, C. Wang, Q. Hou, J. Li, J. Phys. D: Appl. Phys. 40, 7335 (2007).

[34] M.L. Megherbi, F. Pezzimenti, L. Dehimi, A. Saadoune, F.G. Della Corte, J. Electron. Mater. 47, 1414 (2018).

[35] F. Pezzimenti, L.F. Albanese, S. Bellone, F.G. Della Corte, Proc. IEEE Conf. on Bipolar/BiCMOS Circuits and Technology Meeting -BCTM, 214-217 (2009).

[36] M.L. Megherbi, F. Pezzimenti, L. Dehimi, M.A. Saadoune, F.G. Della Corte, IEEE Trans. Electron Dev. 65, 3371 (2018).

[37] F. Pezzimenti, F. G. Della Corte, Proc. Mediterranean Electrotechnical Conf., MELECON, 1129-1134 (2010).

[38] J. Dziewior, W. Schmid, Appl. Phys. Lett. 31, 346 (1977).

[39] K. Zeghdar, L. Dehimi, F. Pezzimenti, S. Rao, F.G. Della Corte, Jpn. J. Appl. Phys. 58, 014002 (2019).

[40] O.K. Jani, Development of wide-Bandgap InGaN solar cells for high-efficiency photovoltaics, PhD Thesis Georgia Institute of Technology (2008).

[41] M. Nawaz, A. Ahmad, Semicond. Sci. Tech. 27, 035019 (2012).

[42] J.F. Muth, A.J. H. Lee, I.K. Shmagin, R.M. Kolbas, H.C. Caser, B.P. Keller, U.K. Mishra, S.P. DenBaars, Appl. Phys. 71, 2572 (1997).

[43] J. Wu, W. Walukiewicz, K.M. Yu, J.W. Ager III, E.E. Haller, H. Lu, W.J. Schaff, Appl. Phys. Lett. 80, 4741 (2002).

[44] M.E. Levinshtein, S.L. Rumyantsev, M.S. Shur, Properties of Advanced Semiconductor Materials, Wiley, Chichester, UK, 2001.